GDCh Research Article Angewandte International Edition Chemie www.angewandte.org

How to cite: *Angew. Chem. Int. Ed.* **2024**, *63*, e202412090
doi.org/10.1002/anie.202412090

Photocatalysis Hot Paper

Exchange of CO_2 with CO as Reactant Switches Selectivity in Photoreduction on Co–ZrO_2 from C_{1-3} Paraffin to Small Olefins

*Tarik Loumissi[+], Rento Ishii[+], Keisuke Hara[+], Tomoki Oyumi[+], Ikki Abe, Chongxu Li, Hongwei Zhang, Rumiko Hirayama, Kaori Niki, Takaomi Itoi, and Yasuo Izumi**

Abstract: Photocatalytic reduction of CO_2 into $C_{2,3}$ hydrocarbons completes a C-neutral cycle. The reaction pathways of photocatalytic generation of $C_{2,3}$ paraffin and C_2H_4 from CO_2 are mostly unclear. Herein, a Co^0–ZrO_2 photocatalyst converted CO_2 into C_{1-3} paraffin, while selectively converting CO into C_2H_4 and C_3H_6 (6.0 ± 0.6 μmol h^{-1} g_{cat}^{-1}, 70 mol %) only under UV/Visible light. The photocatalytic cycle was conducted under ^{13}CO and H_2, with subsequent evacuation and flushing with CO. This iterative process led to an increase in the population of C_2H_4 and C_3H_6 up to 61–87 mol %, attributed to the accumulation of CH_2 species at the interface between Co^0 nanoparticles and the ZrO_2 surface. CO_2 adsorbed onto the O vacancies of the ZrO_2 surface, with resulting COH species undergoing hydrogenation on the Co^0 surface to yield C_{1-3} paraffin using either H_2 or H_2O (g, l) as the reductant. In contrast, CO adsorbed on the Co^0 surface, converted to HCOH species, and then split into CH and OH species at the Co and O vacancy sites on ZrO_2, respectively. This comprehensive study elucidates intricate photocatalytic pathways governing the transformation of CO_2 into paraffin and CO to olefins.

Introduction

In contrast to the irreversible consumption of fossil fuels and raw materials, the conversion of CO_2 reduction into fuels and/or valuable chemicals using a sustainable energy represents a pivotal step toward establishing a new carbon-neutral cycle.[1–2] Photocatalytic CO_2 reduction offers a direct and simple approach; however, the range of products has been limited to CO, CH_4, and CH_3OH,[1–3] unlike the electrochemical production of a broad spectrum including formate,[4] C_2H_6, C_2H_4,[4–5] CH_3CHO,[4] C_2H_5OH,[4–6] C_3H_8, C_3H_6, C_3H_7OH,[4, 6] acetate,[5–6] and oxalate[5] from CO_2 and/or CO, facilitated by concentrated electrons supplied from electricity. The economically viable nature that formed C_2 and C_3 hydrocarbons (HCs) derived from photocatalytic CO_2 reduction (Table S1) has emerged as key chemicals ($0.9–8 \$ kg^{-1}$) compared to CO and CH_4 ($0.06–0.18 \$ kg^{-1}$).[3] Various catalysts have been explored for this purpose, including Co–Cu/TiO_2 for C_2H_6 and C_3H_8;[7] single Au/red P,[8] CdS/Cu–nanotube,[9] Nafion–Pd–TiO_2,[10] Pt–graphene/TiO_{2-x},[11] graphene–TiO_2,[12] and Au@$Bi_{12}O_{17}Br_2$ for C_2H_6;[13] $CuPt_2$/TiO_2 nanotube,[14] Au–Pd/TiO_2 {1 0 1},[15] and $TiON_{1-(O\ vacancy)}$ for C_2H_6 and C_2H_4;[16] C/Cu_2O nanorod,[17] Cu/TiO_2,[18] Ag–C nanotube@TiO_2,[19] CuO/$CuGaS_2$,[20] Bi_2S_3@In_2S_3,[21] $FeCoS_2$,[22] $In_{2.77}S_4$/porous polymer,[23] N, S/Fe–MOF,[24] and $Cu^{\delta+}$/CeO_2–TiO_2 for C_2H_4;[25] forming the corresponding alcohol, aldehyde, and acid.[3, 26–28]

The number of reports on the photocatalytic synthesis of C_2 and C_3 HCs from CO_2 has dramatically increased since 2019 (Table S1a, b, g, i, j, and n–s), yet a comprehensive understanding of the reaction pathways remains elusive, hindering precise control. This study reports the switchover of photocatalytic pathways from CO_2 to C_{1-3} paraffin versus from CO to selective C_2H_4 and C_3H_6, using a Co^0–ZrO_2 catalyst (Supporting Information, *1.2. Major Framework of This Study*).

Results and Discussion

Photocatalytic $^{13}CO_2$ Reduction Using H_2. The photocatalytic reduction tests of $^{13}CO_2$ were first performed using ZrO_2–823R, Co–ZrO_2–823R (where 823 denotes the pre-treatment temperature (K) of the photocatalysts with H_2 and R represents reduced), and a Xe arc lamp guided through a quartz light conduit (142 mW cm^{-2}; Table 1a–i). ZrO_2 mostly reflected/scattered $94.5 \% \pm 0.3 \%$ of light (300 nm < wavelength λ < 2800 nm), while Co–ZrO_2-fresh, −723R, and −973R mostly absorbed $93.2 \% \pm 0.5 \%$, $93.2 \% \pm 0.3 \%$, and $97.2 \% \pm 0.2 \%$ of light, respectively (SI, *2.*

[*] T. Loumissi,[+] R. Ishii,[+] Dr. K. Hara,[+] T. Oyumi,[+] I. Abe, C. Li, Prof. Dr. H. Zhang, R. Hirayama, Prof. Dr. K. Niki, Prof. Dr. Y. Izumi
Department of Chemistry, Graduate School of Science
Chiba University
Yayoi 1–33, Inage-ku, Chiba 263-8522, Japan
E-mail: yizumi@faculty.chiba-u.jp

Prof. Dr. T. Itoi
Department of Mechanical Engineering, Graduate School of Engineering
Chiba University
Yayoi 1–33, Inage-ku, Chiba 263-8522, Japan

[+] T.L., R.I., and T.O. shared experiments and K.H. contributed for calculations equally to this paper all in the graduate course.

Table 1: Kinetic Data for Photoconversion of CO_2 or CO Using Co (7.5 wt%)–ZrO_2 Photocatalysts Irradiated under UV/Visible Light.

Entry	C oxide	Reductant	T (K) under H_2	Light intensity	Formation rate (μmol h^{-1} g_{cat}^{-1})							
					^{13}CO	$^{13}CH_4$	$^{12}CH_4$	$^{13}C_2H_4$	$^{13}C_2H_6$	$^{13}C_3H_6$	$^{13}C_3H_8$	$^{16}O_2$
a	$^{13}CO_2$ (2.3 kPa)	H_2 (21.7 kPa)	–	142 mW per 1 cm^2-cat[*1]	0.016[*3]		< 0.002	< 0.002	< 0.002	< 0.002	< 0.002	< 0.002
b			723		0.29[*3]	1.1	0.14		0.011			
c			823		3.6[*3]	300	23		4.1		0.41	
d			973		11[*3]	190	8.9		3.4		0.25	
e		H_2 (2.3 kPa)			40	52	3.3		1.1		0.082	
f		H_2O (2.2 kPa)	823		2.6	16	3.4		0.20		0.014	
g	^{13}CO (2.3 kPa)	H_2 (2.3 kPa)			–	15	1.1	5.5[*2]	0.70		0.098	< 0.002
h		H_2 (21.7 kPa)	973			8.6	1.9	0.061	1.3	0.67	1.7	
i		H_2 (2.3 kPa)				2.2	0.18	5.2[*4]	0.23	0.74[*4]	0.024	
					CO	CH_4		$^{12}C_2H_6$			$^{12}C_3H_8$	O_2
j[*5]	CO_2 (95 kPa)	H_2O (70 mL)	973	90.2 mW per flask[*2]	0.90	0.25		0.071		0.024		110
k[*5]			823	222 mW per flask[*2]	41	8.8		1.6		1.0		590
l[*5]			973		19	3.4		1.5		0.52		66

[*1] Using a quartz reactor (Chart S1). [*2] Using a Pyrex flask equipped with quartz window (Chart S2). [*3] Formation ceased within 1–4 h of reaction owing to the subsequent consecutive reactions. [*4] Selected consecutive reactions with the highest rates. [*5] Photocatalyst quantities were 20 mg each, except for entries j (9.0 mg), k (3.5 mg), and l (16 mg).

Experimental Section). In contrast to the sluggish formation of ^{13}CO using ZrO_2–823R (Table S3a), the utilization of Co–ZrO_2–823R comprising 2.5–10 wt % of Co resulted in the predominant formation of $^{13}CH_4$ accompanied by $^{12}CH_4$, $^{13}C_2H_6$, ^{13}CO, and $^{13}C_3H_8$ (Tables 1c and S3c–e and i). ^{13}CO emerged as the primary product within 5 h of the reaction, followed by $^{13}C_{1-3}$ paraffin formation (Figure 1). Among these catalysts, Co (7.5 wt %)–ZrO_2–823R exhibited the highest total formation rate of HCs and CO (Tables 1c and S3e and Scheme S1A). This study confirmed a similar distribution of C_{1-3} paraffin distribution using Co–Cu/TiO_2 (Table S1a)[7] via monitoring of ^{13}C-isotopic time-course dynamics.

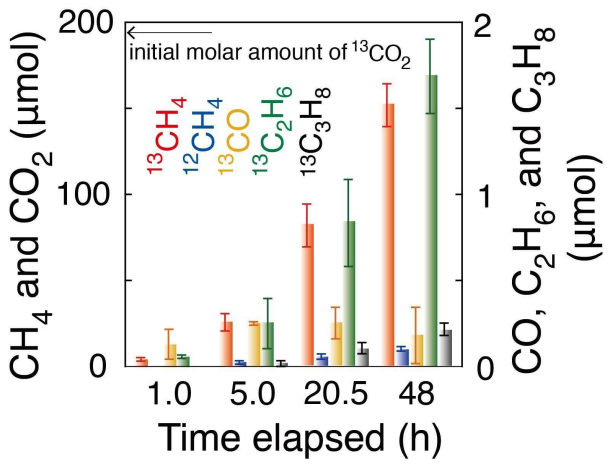

Figure 1. Time–course formation of photocatalytic $^{13}CH_4$, $^{12}CH_4$, ^{13}CO, $^{13}C_2H_6$, and $^{13}C_3H_8$ during exposure to $^{13}CO_2$ (2.3 kPa) and H_2 (21.7 kPa) irradiated under UV/Visible light (142 mW cm^{-2}) using Co (7.5 wt%)–ZrO_2 (0.020 g) treated in H_2 at 823 K. The error bars for each product were evaluated based on three factors described in SI, *3.1. Kinetic Results.*

The performance of nonheated Co (7.5 wt %)–ZrO_2 under H_2 was even poorer than ZrO_2 (Tables 1a and S3a). This aligns with previous findings on photocatalytic CO formation using CO_2 and Co_3O_4 nanoparticles, which necessitated a Ru photosensitizer and triethanolamine.[29] Next, the reduction temperature in H_2 of the Co (7.5 wt %)–ZrO_2 photocatalyst was varied between 723 and 973 K (Figure S2A–C and Table 1b–d). The major $^{13}CH_4$ formation rate increased by 280 times with Co–ZrO_2–823R compared to –723R. However, this rate dropped to 63 % with Co–ZrO_2–973R compared to that using –823R, owing to the progressive reduction from Co_3O_4 to metallic Co^0 and the possibly superior reactivity of the face-centered cubic (fcc) Co^0 surface versus hexagonal close-packed (hcp) one[30] (see the following *UV/Visible spectra, high-resolution transmission electron microscopy (HR-TEM), and X-ray absorption near-edge structure (XANES)* sections). More than 87 % of the formation rates were retained in repeated photocatalytic tests (Figure 1), provided that adsorbent balance on the Co^0 surface was maintained (SI, *3.1. Kinetic Results*).

The obtained molar ratio of C_{1-3} paraffin ($^{13}CH_4$, $^{12}CH_4$, $^{13}C_2H_6$, to $^{13}C_3H_8$) was almost constant at 100: 4.7–13: 0.98–1.8: 0–0.14 (Table 1b–d), regardless of the reduction temperature under H_2. This consistency suggests a common reaction pathway, independent of the reduction temperature

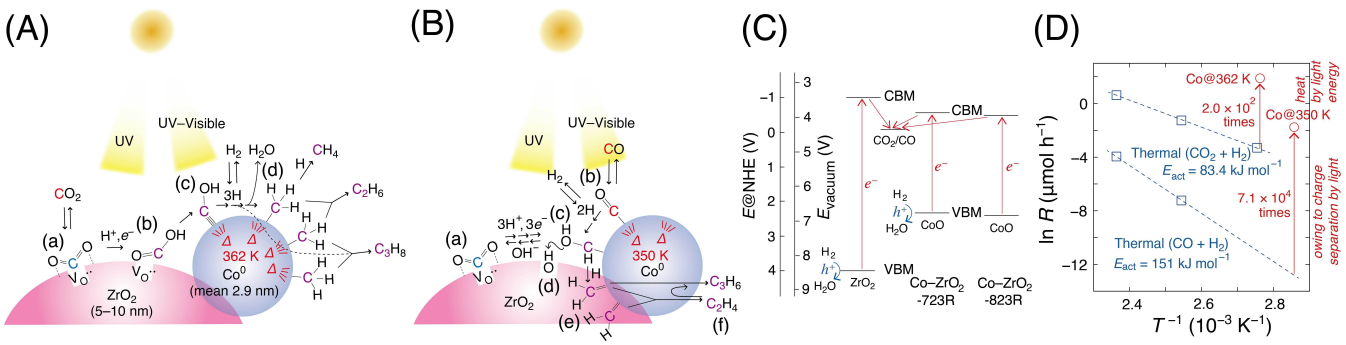

Scheme 1. (A, B) Proposed Mechanisms for CO_2 Photoreduction to C_{1-3} Paraffin (A) and CO Photoreduction to $C_{2,3}$ Olefins (B); (C) the Energetics of First Half of Photocatalytic Reaction Steps from CO_2 to CO and the Electron Flows; and (D) Comparisons of $^{13}CO_2$ and ^{13}CO Reduction Rates between Photocatalytic (circle, ○) versus Thermal (square, □) Processes Using Co–ZrO_2–823R for $^{13}CO_2$ and Co–ZrO_2–973R for ^{13}CO Reduction.

(Scheme 1A). The considerably slow dissociation of the first C–O bond in the CO_2-derived intermediate on O vacancy ($Vo^{\bullet\bullet}$) sites at the ZrO_2 surface (Scheme 1A–b, c) is likely rate-limiting,[31] thereby determining the overall rates. We previously reported the photocatalytic roles of $Vo^{\bullet\bullet}$ sites on CO_2 photoreduction.[31] Subsequent steps from COH involve common progressive hydrogenation toward C_{1-3} paraffin over Co^0 sites, resulting in a very similar paraffin ratio (Figure S2A–C and Scheme 1A–c, d; see the following *density functional theory (DFT) calculations* section).

Even when only visible light was utilized for irradiation, the C_{1-3} paraffin ratio remained consistent, suggesting a similar reaction pathway involving the utilization of $Vo^{\bullet\bullet}$ sites at the ZrO_2 surface (Table S3e, g, and h; SI, *3.1. Kinetic Results*).

Photocatalytic ^{13}CO Reduction. The CO photoreductions were tested using the most active Co (7.5 wt %)–ZrO_2–823R compared to the CO_2 photoreduction reactions (Scheme S1A). When ^{13}CO (2.3 kPa), H_2 (2.3 kPa), and UV/Visible irradiation were used, $^{13}C_2H_4$ became the second major product (24 mol %) following $^{13}CH_4$ (67 mol %; Figure S3 and Table 1g). $^{13}C_2H_4$ was the primary product, followed by secondary $^{13}C_2H_6$ evolution after 5 h of reaction, demonstrating a consecutive first-order reaction kinetic model (Eq. S5 and Figure S4), with a CH_2 intermediate, followed by C_2H_4, then C_2H_6 generations. The discrepancy between the amount of CO lost and the amount of products was mostly due to bidentate formate formation on ZrO_2 surface[32] (see *Reaction Mechanism* section and Figure S16) because formic acid and C_{1-3} alcohols were not found and negligible change of OH stretching vibration region in Fourier transform infrared (FTIR) spectra under the photocatalytic conditions. The molar ratio of C_{1-3} HC formation rates, $^{13}CH_4$, $^{12}CH_4$, $^{13}C_2H_4$, $^{13}C_2H_6$, to $^{13}C_3H_8$, was determined to 100: 7.2: 36: 4.6: 0.64 for photoreduction starting from ^{13}CO (2.3 kPa) and H_2 (2.3 kPa), differing from the values of 100: 7.7: 0: 1.4: 0.14 for photoreduction starting from $^{13}CO_2$ (2.3 kPa) and H_2 (21.7 kPa) (Table 1c and g). In the photocatalytic test using CO_2 and H_2, CO was negligibly identified as the intermediate, suggesting either its absence in the reaction pathway or the presence of a specific active site that selectively activates CO over CO_2. While this aspect has been discussed for CO_2 electroreduction,[4] it has received limited attention in CO_2 photoreduction.[3]

Furthermore, using the Co (7.5 wt %)–ZrO_2–973R photocatalyst, ^{13}CO (2.3 kPa), H_2 (2.3 kPa), and UV/Visible light (Figure 2) resulted in olefins as the major products: $^{13}C_2H_4$ (61 mol %) and $^{13}C_3H_6$ (8.6 mol %), rather than $^{13}CH_4$ (25 mol %; Table 1i and Scheme S2B). The formation rate (5.2 ± 0.5 μmol h^{-1} g_{cat}^{-1}) and selectivity (61 mol %) of $^{13}C_2H_4$ are comparable to those reported in 2023 (12–68 μmol h^{-1} g_{cat}^{-1}, 11–86 mol %; Table S1n–r).[20–24] However, the photocatalytic C_3H_6 formation (0.74 μmol h^{-1} g_{cat}^{-1}) from CO and/or CO_2 is uncommon, with $^{13}C_2H_4$ being formed first, followed by $^{13}C_2H_6$, then $^{13}C_3H_6$ and $^{13}C_3H_8$ in consecutive order (Figure 2). Such consecutive reactions were well reproduced.

$^{12}CH_4$ originated from $^{12}CO_2$ in the air, which chemisorbed onto $Vo^{\bullet\bullet}$ sites at the ZrO_2 surface.[31–33] This was confirmed by X-ray photoelectron spectroscopy upon the

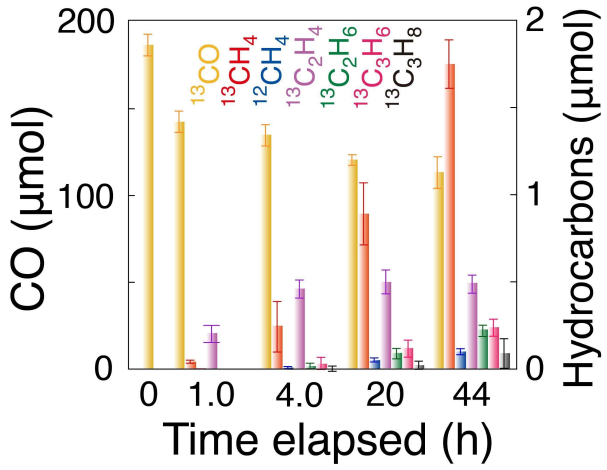

Figure 2. Time–course formation of photocatalytic $^{13}CH_4$, $^{12}CH_4$, $^{13}C_2H_4$, $^{13}C_2H_6$, $^{13}C_3H_6$, and $^{13}C_3H_8$ and the decrease of ^{13}CO during exposure to ^{13}CO (2.3 kPa) and H_2 (2.3 kPa) irradiated under UV/Visible light (142 mW cm^{-2}) using Co (7.5 wt %)–ZrO_2 (0.020 g) treated in H_2 at 973 K. The error bars for each product were evaluated based on three factors described in SI, *3.1. Kinetic Results*.

introduction of CO_2 and H_2 to Co–ZrO_2–823R (Figure S8A and B): the positive shift of Zr 3d peak indicating more Zr^{4+} population (+0.14 eV, panel A) shifted from Zr^{3+} associated with $Vo^{\bullet\bullet}$ site and the growth of O (surface) peaks in the region 535.5–531.5 eV compared to O (lattice) at 530.1 eV in O 1s region (panel B).

The ratio of $^{12}CH_4$ among the total CH_4 formed did not align with the impurity ratio of $^{12}CO_2$ in the $^{13}CO_2$ reagent used (1 %) but instead ranged from 4.5 % to 12 % during the tests using $^{13}CO_2$ and H_2 (Table S4b–e). This suggests that gas-phase $^{13}CO_2$ was in equilibrium with chemisorbed $^{12}CO_2$ on $Vo^{\bullet\bullet}$ sites at the ZrO_2 surface from the air (Scheme 1A–a). When ^{13}CO and H_2 were used, the ratio of $^{12}CH_4$ among the total CH_4 formed was 6.7–18 % (Table S4g–i). Thus, gas-phase ^{13}CO was also in equilibrium with chemisorbed $^{12}CO_2$ on $Vo^{\bullet\bullet}$ sites via Eqs. 1 and 2.

$$^{13}CO + X\ (ZrO_2\ \text{surface}) \rightleftharpoons {}^{13}COX\ (ZrO_2\ \text{surface}) \quad (1)$$

$$^{13}COX\ (ZrO_2\ \text{surface}) + {}^{12}CO_2\ (Vo^{\bullet\bullet}\text{site}) \rightleftharpoons {}^{12}COX + {}^{13}CO_2\ (Vo^{\bullet\bullet}\text{site}) \quad (2)$$

One possibility of such equilibrium is shown in Scheme 1B–a–c via HCOH species (X=2H in Eq. 1). Such photocatalytic reaction pathway is specific in contrast to thermal CO_2 conversion, which predominantly occurs over the Co^0 surface at temperatures higher than 425 K (SI, *3.1. Kinetic Results*).[3]

Switching Photocatalytic ^{13}CO Reduction. We attempted to extract the first selective step of C_2H_4 and C_3H_6 formation in consecutive photocatalysis using ^{13}CO, H_2, and the optimal Co (7.5 wt %)–ZrO_2–973R photocatalyst (Scheme S1B) by switching the reaction gases as follows: (i) under ^{13}CO (2.3 kPa) and H_2 (2.3 kPa) for 4 h, (ii) under vacuum for 1 h, then (iii) under ^{13}CO (2.3 kPa) for 1 h. These steps were repeated (Figure 3). At step i of the first cycle, the molar ratio of olefin ($^{13}C_2H_4$ and $^{13}C_3H_6$) formation was measured as 57 mol % after 4 h of reaction, similar to the initial stage of Figure 2.

The control key for the selective formation of C_2H_4 and C_3H_6 was the concentration of CH_2 intermediate on the Co surface (Scheme 1B–e and Figure S4), which progressively decreased, resulting in the switching from $C_{2,3}$ olefin to paraffin formation within 4 h of photoreaction. The HC intermediates on the Co surface were effectively removed under vacuum conditions (Scheme 1B–e and f), followed by ^{13}CO adsorption during steps ii and iii (Figure 3).

In the second cycle, at step i, the total formation rate after 4 h of reaction was 84 mol % of that observed in the first cycle. The molar ratio of olefin formation was 57 mol %. Subsequently, in the third cycle, at step i, the total formation rate after 4 h of reaction decreased to 69 mol % of the first cycle, with the olefin formation molar ratio measured at 60 mol %. Furthermore, in the fourth cycle, at step i, the total formation rate after 4 h of reaction was 62 mol % of that observed in the first cycle, with the olefin formation molar ratio of 61 mol %.

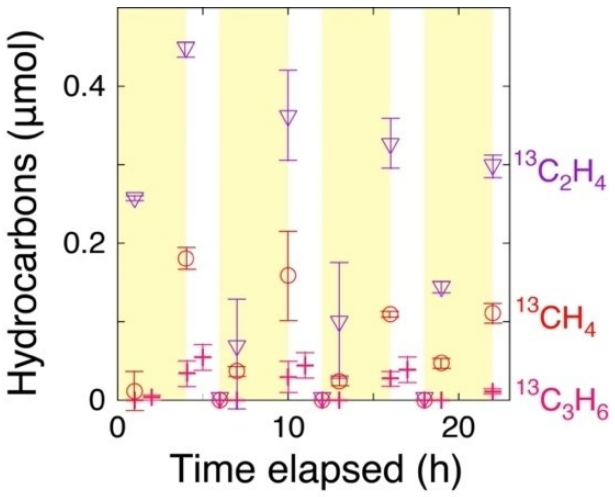

Figure 3. Time–course formation of photocatalytic $^{13}CH_4$, $^{13}C_2H_4$, and $^{13}C_3H_6$ (i) during exposure to ^{13}CO (2.3 kPa) and H_2 (2.3 kPa) for 4 h, followed by (ii) 1 h of evaluation and (iii) subsequent exposure to ^{13}CO (2.3 kPa) for 1 h using Co (7.5 wt %)–ZrO_2–973R (0.020 g) irradiated under UV/Visible light (142 mW cm^{-2}). The cycle of steps (i)–(iii) was repeated four times. The error bars for each product were evaluated based on three factors described in SI, *3.1. Kinetic Results.*

The switching olefin photoformation was nicely reproduced in separated test under ^{13}CO and H_2, vacuum, then ^{13}CO (Figure S5); olefin formation molar ratio gradually increased from 70 to 77, 83, and 87 mol % while total formation rate gradually decreased from 100 to 99, 68, and 55 mol %. Due to the nature of consecutive reaction, olefin selectivity critically depended on time exposed to ^{13}CO, H_2, and UV/Visible light (4–10 h). Upon repetition of the cycle, the ratio of $^{13}C_2H_4$ and $^{13}C_3H_6$ among all the HCs increased owing to the gradual accumulation of CH_2 and/or C_2H_4 intermediate species (Scheme 1B–e) over the Co^0 surface compared to CO and CH_3 species, even after flushing under vacuum and exposure to ^{13}CO between cycles (see following *FTIR spectroscopy* section). Thus, the first step of the consecutive photocatalytic CO reduction, i.e. $C_{2,3}$ olefin formation, using the Co (7.5 wt %)–ZrO_2–973R photocatalyst was successfully extracted.

Pressure Dependence of $^{13}CO_2$/^{13}CO Reduction and $^{13}CO_2$ Uptake/Exchange. To provide insights into reaction mechanism, the pressure dependence of the reactant was considered. Using Co (7.5 wt %)–ZrO_2–973R (Scheme S1B), $^{13}CO_2$ (2.3 kPa), and H_2 (2.3–21.7 kPa), the formation rate ratio of $^{13}CH_4$, $^{12}CH_4$, $^{13}C_2H_4$, $^{13}C_2H_6$, $^{13}C_3H_6$, to $^{13}C_3H_8$ was essentially constant: 100:4.7–6.4:0:1.8–2.2:0:0.13–0.16 (Table 1d and e), indicating no competition between CO_2 and H_2 for adsorption. In contrast, using CO (2.3 kPa) and H_2 (2.3 kPa), the ratio was skewed toward olefin selectivity, measuring 100:8.6:243:11:34:1.1, which differs from the 100:23:0.71:15:7.8:20 observed with CO (2.3 kPa) and H_2 (21.7 kPa; Table 1h and i). This suggests that the surface concentration of CH_2 species critically depended on H concentration (Scheme 1B–e). Conversely, high H_2 pressure decreased the ^{13}CO formation rate using $^{13}CO_2$ and ZrO_2

(Table S3a and b), suggesting competitive adsorption of CO_2 on $Vo^{\bullet\bullet}$ sites and H on neighboring Zr sites.[31]

Then, the CO_2 adsorption sites were investigated using $^{13}CO_2$ uptake and exchange reactions with Co (7.5 wt %)–ZrO_2–823R (Scheme S1A) and UV/Visible light irradiation (Figure 4). At a rate constant of 4.7 h^{-1}, the initial rapid uptake of $^{13}CO_2$ and 1.0 % impurity $^{12}CO_2$ (in total 19.0 μmol) were attributed to physisorption on the ZrO_2 surface. The additional uptake (9.1 μmol) of CO_2 compared to the 9.9 μmol-CO_2 using the same amount (20 mg) of undoped ZrO_2 catalyst (Table S5a and b)[32] corresponded to 36 mol % of the Co-site in the Co (7.5 wt %)–ZrO_2–823R catalyst. Thus, rapid CO_2 adsorption on Co^0 was implausible, and the extra uptake was attributed to the formation of Co carbonate resulting from the reaction of CoO with CO_2.

Subsequent $^{13}CO_2$ uptake on the Co (7.5 wt %)–ZrO_2–823R was also physisorption at a rate constant of 0.4 h^{-1} (Figure 4 and Table S5b), suggesting adsorption at the interface sites. Conversely, the much slower $^{13}CO_2/^{12}CO_2$ exchange reaction, with a rate constant of 0.2 h^{-1}, was attributed to the chemisorption site, likely owing to the presence of $Vo^{\bullet\bullet}$ sites. In this mechanism, the $^{12}CO_2$ adsorbed from the air is exchanged with gas-phase $^{13}CO_2$ (Scheme 1A–a). The concentration was calculated to be one vacancy per a ZrO_2 surface area of 61 nm^2, in consistent with the total amount of $^{12}CH_4$ formed using N_2, H_2, and UV/Visible light irradiation (Table S3f and SI, *3.1. Kinetic Results*).

Electronic Characterizations. Diffuse-reflectance UV/Visible spectra were measured to monitor effective electrons by changing the reduction temperature of photocatalysts. In addition to the absorption edge observed at 248 nm for ZrO_2 (Figure S6A–a), two peaks appeared at 387 and 687 nm for the fresh Co (7.5 wt %)–ZrO_2 (spectrum b), attributed to the charge transfer from O^{2-} to Co^{2+} and O^{2-} to Co^{3+}, respectively, in Co_3O_4.[34–35] For Co (7.5 wt %)–ZrO_2–723R, a single peak appeared at 612 nm owing to the charge transfer from O^{2-} to Co^{2+} in CoO (spectrum c).[35] Based on the fitting of these spectra to the equation proposed by Davis and Mott,[36]

$$\alpha \times h\nu \propto (h\nu - E_g)^n, \quad (3)$$

where h is Planck constant, ν is the frequency of light, and α is a constant, band gap E_g values of 2.4 and 2.9 eV were obtained for allowed direct transition ($n = 1/2$)[35] in Co_3O_4 and CoO nanoparticles over ZrO_2 (Figure S7A and B and Scheme 1C), respectively.

The absorption in the range of 250–800 nm progressively increased with the elevation of the reduction temperature to 823 K and then to 973 K (Figure S6A–d and e), suggesting a complete reduction to metallic Co^0 at 973 K, in accordance with the findings in the following *XANES/extended X-ray absorption fine structure (EXAFS)* sections. However, the peak observed at 612 nm attributable to CoO (15 mol %) (intensity ~0.05) was not well resolved, as it overlapped with the absorption by Co^0 (85 mol %, intensity 2–3) for Co (7.5 wt %)–ZrO_2–823 R (see *XANES* section).

The energetics of the Co–ZrO_2 photocatalysts are summarized in Scheme 1C. Concerning the valence band maximum (VBM) of ZrO_2 (4.0 V vs. normal hydrogen electrode, NHE), the band gap value was 5.0 eV based on the UV/Visible spectrum (Figure S6A–a), while the conduction band minimum (CBM) was at −1.0 V vs. NHE. The VBM values of CoO in Co (7.5 wt %)–ZrO_2–723 R and −823R photocatalysts were calculated to 2.3 and 2.4 V vs. NHE (Scheme 1C), respectively (Figure S8C and SI, *3.2. Characterizations*).

Based on the band gap values for CoO (2.9 eV) shown in Figure S7B, its CBMs were at −0.6 and −0.5 V (SI, *3.2. Characterizations*). Thus, UV and/or visible light-excited electrons to the CB of both ZrO_2 and CoO could thermodynamically reduce CO_2 to CO (−0.11 V; Scheme 1C). Thus, the presence of CoO adjacent to Co^0 nanoparticles can boost CO_2 photoreduction by leveraging visible light.

The efficiency of charge separation in photocatalysts by light was evaluated by fluorescence spectroscopy (Scheme S1C). The fluorescence peak intensity associated with the near band-edge and the midgap trap states was suppressed to one-tenth to one-fifth for Co (7.5 wt %)–ZrO_2 compared to corresponding peaks for ZrO_2 owing to the charge transfer of light-excited electrons to Co_3O_4, CoO, or Co^0. The associated peaks in excitation spectra were substantially suppressed owing to the charge transfer effect to Co species in accordance with fluorescence spectra (Figure S6B and C; SI, *3.2. Characterizations*) and in-profile CO_2 photoreduction tests suggested an auxiliary role of vacancy/impurity level of ZrO_2 (SI, *3.1. Kinetic Results*), suggesting the utilization of the charges for photocatalysis.[1–2]

Structural Characterizations. The morphology of the Co (7.5 wt %)–ZrO_2–723R (Figure S9), −823R, and −973R samples (Figure 5) was observed using HR-TEM to provide structural information on nano level and the changes of

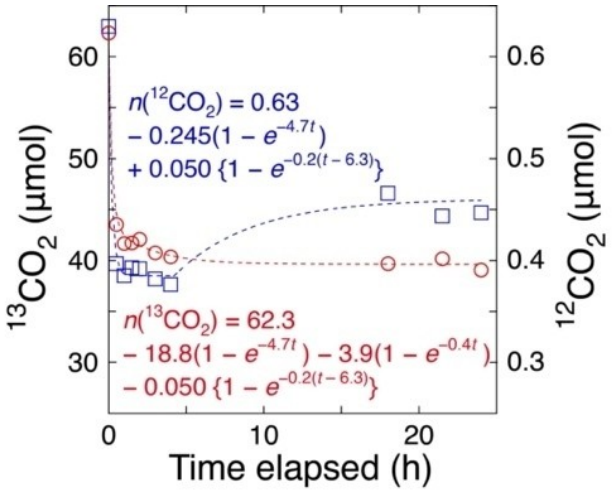

Figure 4. Time–course uptake and exchange reaction of $^{13}CO_2$ (0.68 kPa) under UV/Visible light irradiation (142 mW cm^{-2}) using Co (7.5 wt %)–ZrO_2–823R and the fit equation curves based on first order kinetics. The amount of catalyst is 0.020 g.

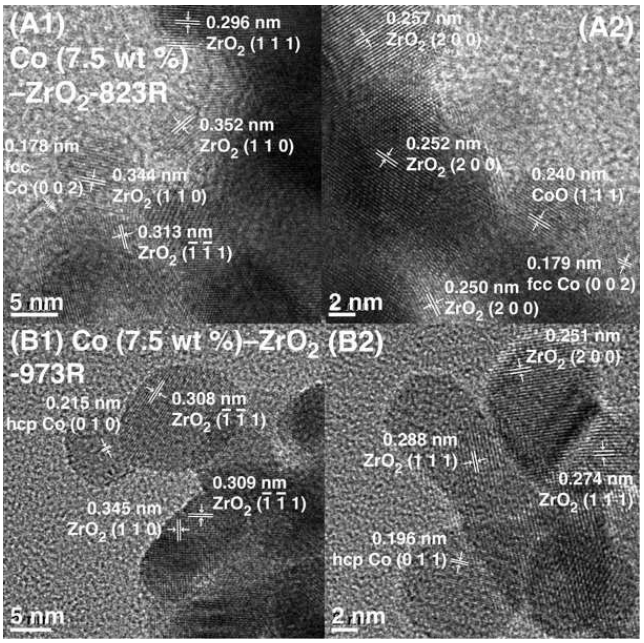

Figure 5. HR-TEM images of Co (7.5 wt%)–ZrO_2–823R (A1, A2) and Co (7.5 wt%)–ZrO_2–973R photocatalysts (B1, B2). Lattice intervals for monoclinic ZrO_2 (all panels), CoO (A2), fcc Co (A1, A2), and hcp Co (B1, B2) were also drawn.

especially Co sites owing to reduction temperature (Scheme S1C). The monoclinic phase of ZrO_2 crystals with 5–10 nm (Scheme 1) in size was preferably observed, exhibiting lattice fringes with the intervals of 0.274–0.296, 0.344–0.352, 0.246–0.257, 0.240, 0.264–0.267, and 0.308–0.313 nm corresponding to ZrO_2 (1 1 1), (1 1 0), (2 0 0), (0 2 1), (0 0 2), and ($\bar{1}$ $\bar{1}$ 1) (theoretical values 0.285, 0.365, 0.255, 0.234, 0.264, and 0.318 nm),[32–33] respectively, for these three samples.

In contrast to Co (7.5 wt %)–ZrO_2–723R, where cubic CoO was observed (1 1 1) lattice interval = 0.247 nm, theoretical = 0.245 nm; (0 0 2) lattice interval = 0.205–0.206 nm, theoretical = 0.212 nm)[37] (Figure S9), for Co (7.5 wt %)–ZrO_2–823R, fcc Co nanoparticles were observed (0 0 2) lattice interval = 0.178–0.179 nm, theoretical = 0.177 nm)[37] in the proximity to CoO nanoparticles comprising (1 1 1) lattice with an interval of 0.240 nm,[38] as shown in Figure 5A2. Furthermore, for Co (7.5 wt %)–ZrO_2–973R, hcp Co nanoparticles were frequently observed with intervals of 0.215 and 0.196 nm corresponding to the (0 1 0) and (0 1 1) lattices (Figure 5B1, 2; theoretical = 0.217 and 0.192 nm),[39] respectively, while no CoO phase was observed. A few nanometer-sized Co nanoparticles could exhibit fcc packing owing to the reduction at 823 K, while many Co crystals (> 5 nm) grown at 973 K transformed into a stable hcp phase. The HR-TEM results were well consistent with the X-ray diffraction (Figure S10A), which showed diffractions from monoclinic ZrO_2. However, only very weak traces of the shoulder owing to hcp Co (0 1 0) and (0 0 2) were identified (Figure S10B) because of their small size of a few nanometers.

Co K-edge XANES spectra confirmed the speciation of Co: Co_3O_4, CoO, and Co^0 metal for fresh Co (7.5 wt %)–ZrO_2, Co (7.5 wt %)–ZrO_2–723R, and −973R, respectively (Figure S11A and SI, *3.2. Characterizations*), consistent with UV/Visible absorption spectroscopy (Figure S6A). For Co (7.5 wt %)–ZrO_2–823R, the Co site comprised a mixture of CoO (15 %) and Co^0 (85 %) (Figure S11B). The CoO amount based on rapid CO_2 physisorption (extra 9.1 μmol of CO_2 corresponding to CoO 36 %; Table S5a and b) was greater than 15 %, evaluated through XANES, probably because slower CO_2 physisorption at the interface between Co and ZrO_2 surface was also included.

In the comparison between Co state and photocatalytic CO_2 reduction, while the fresh Co (7.5 wt %)–ZrO_2 and Co (7.5 wt %)–ZrO_2–723R photocatalysts comprising Co_3O_4 and CoO, respectively (Figure S11A), exhibited poor activity for CO_2 photocatalytic reduction (Tables 1a and b and Figure S2A), Co (7.5 wt %)–ZrO_2–823R and −973R comprising metallic Co (Figure S11A) were the most and the second most active in the CO_2 photocatalytic reduction (Scheme S1A and B, Table 1c and d, and Figures 1 and S2 C), respectively. Thus, metallic Co sites played an essential catalytic role combined with $Vo^{\bullet\bullet}$ sites at ZrO_2 surface[31–33] as dual active sites, similar to our previous reports for Ni–ZrO_2 by experiments[32] and DFT calculations.[31] Three plausible reasons can be listed: (i) fcc Co^0 surface was more conducive to dissociating COH species than hcp one,[30] (ii) CoO could work as a promoter in contact with Co^0 (Figure 5A2) owing to visible light absorption and charge separation with an E_g value of 2.9 eV (Figures S6A–c and S7B and Scheme 1C), and (iii) Co^0 particle size may increase at 973 K. However, the major reason cannot be identified because these potential changes occurred simultaneously at 973 K, and the Co^0 particle size mixed with CoO at 823 K was difficult to determine via EXAFS and HR-TEM (Figure 5A).

Photothermal Monitoring and the Control Thermal $^{13}CO_2/^{13}CO$ Reduction. Related to the latter reaction steps of CO_2 photoreduction over Co sites followed by CO_2 activation at $Vo^{\bullet\bullet}$ sites on ZrO_2 surface, the local electronic and geometric structures associated with the thermal behavior of active metallic Co sites essential for CO_2 photoreduction were monitored via Co K-edge EXAFS spectroscopy. The analysis was conducted under UV/Visible light irradiation using CO_2 (2.3 kPa), H_2 (21.7 kPa), and Co (7.5 wt %)–ZrO_2–973R. To precisely analyze Co^0 sites not mixed with CoO, the second-best catalyst was chosen (Table 1d and Scheme S1B). In the Fourier transform of EXAFS before UV/Visible light irradiation, the curve-fit analysis revealed an intense peak observed at 0.21 nm (uncorrected for phase shift; Figure S12). This peak demonstrated a Co–Co interatomic distance (R) of 0.249 nm with an associated coordination number (N) of 9.8. Furthermore, the N and R values did not change considerably during the photocatalytic reaction (Figure S13A and B). The N value corresponds to a particle size of 2.9 nm, assuming a spherical fcc nanoparticle model with a surface dispersion (D) was 0.43.[40]

The Debye–Waller factor (σ) was calculated using the correlated Debye model[41–42] for bulk and surface Co sites (vertical motion versus surface),[32–33] considering the Debye temperature for bulk $\theta_{D(Bulk)}$ (445 K)[43] and surface $\theta_{D(Surface,\perp)}$ for the vertical motion of freedom (211 K;[44] Figure S1). We approximated the mean temperature of Co nanoparticle ($T_{nanoparticle}$) as the arithmetic mean value, considering $\theta_{D(Surface,\perp)}$ weighted using $\frac{1}{2}\cdot 1/3\ D$ for vertical translational motion at a free hemisphere surface and $\theta_{D(Bulk)}$ weighted using $(1-D)+(1/2)D+(1/2\cdot 2/3)D$ for the bulk site, nonfree hemisphere in contact with ZrO_2 surface, and horizontal translational motion at a free hemisphere surface.

$$T_{nanoparticle} = T_{Surface,\perp} \times (1/6)D + T_{Bulk} \times (1-(1/6)D) \quad (4)$$

The σ value for samples (σ_{sample}) was calculated using Eq. 5, taking the contribution of structural disorder ($\sigma_{disorder}$) and the difference of the σ_{sample} value from the Co metal foil (σ_{XDAP}) into account:

$$\sigma_{sample}{}^2 = \sigma_{Co\ metal,\ correlated\ Debye}{}^2 + \Delta(\sigma_{disorder}{}^2) + \Delta(\sigma_{XDAP}{}^2) \quad (5)$$

At 296 K, σ_{sample} and $\sigma_{Co\ metal,\ correlated\ Debye}$ values were 0.007 (28) and 0.007 (05) nm, respectively, for the nanoparticle model above based on the correlated Debye model (Figure S1) and Eq. 4. The σ_{XDAP} value was given as −0.000 (32) nm. Thus, $\sigma_{disorder}$ was evaluated as 0.001 (82) nm using Eq. 5.

Then, the temperature of the Co site was inversely evaluated based on the σ_{sample} value obtained from Eq. 5 and the arithmetic mean value based on Eq. 4 (Figure 6). This specific approach directly monitored the local Co site temperature.[32–33] The Co sites were initially at 296 K before exposure to UV/Visible light. Upon irradiation, the temperature of the Co sites quickly increased to 362 ± 21 K, gradually decreasing once the light was turned off after 138 min. The gradual drop in temperature post-illumination cessation (Figure 6) is probably attributed to the presence of a minor CoO layer between the Co^0 nanoparticle and the ZrO_2 surface, which slows heat dissipation.

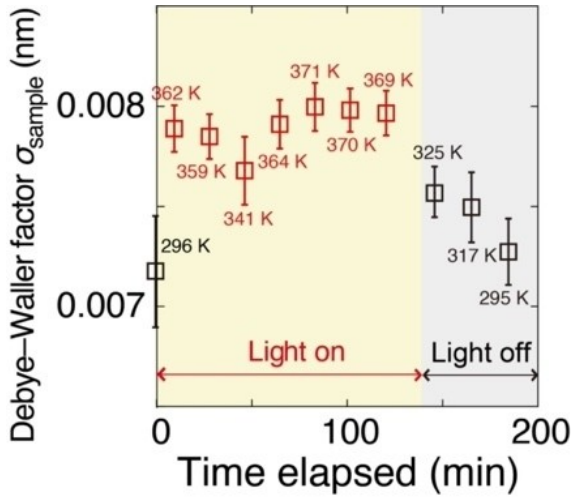

Figure 6. Time course of the Debye–Waller factor σ derived from the Co K-edge EXAFS analysis and the determined temperature of Co nanoparticles in Co (7.5 wt%)–ZrO_2–973R using CO_2 (2.3 kPa), H_2 (21.7 kPa), and UV/Visible light irradiation (142 mW cm^{-2}), based on the correlated Debye model. The error bars were drawn based on data reproducibility in three runs and the fit errors.

Compared with the critical change of σ_{sample} values triggered by UV/Visible light irradiation (Figure 6), the N(Co–Co) and R(Co–Co) values negligibly varied during UV/Visible light exposure and cessation, except for rapid initial quick changes upon the light activation (Figure S13). This initial change may result from the oxidation of minor Co^{II} sites by the effect of CO_2 (Figure S11B), which were subsequently reduced under H_2 and UV/Visible light. The reduced state of Co^{II} maintained a dynamic equilibrium under these conditions, with N values gradually decreasing upon light deactivation (Figure S13A).

The CH_4 formation rate reached 196 μmol h^{-1} g$_{cat}{}^{-1}$ (Table 1d) under UV/Visible light irradiation leading to a temperature rise of 11.9 K within 10 min thermodynamically. However, this increase was smaller than the initial observed increase of 66 K within 10 min (Figure 6; SI, *3.2. Characterizations*). Thus, the temperature elevation in Figure 6 stemmed from the transformation of light energy into heat at the Co^0 surface, quickly reaching the heat equilibrium and dissipating into the reactor/EXAFS cell.

Consistent with this evaluation of warming of Co^0 sites by light under CO_2, the time course of Fourier transform (Figure S14), σ value, and Co^0 site temperature under CO, H_2, Co (7.5 wt %)–ZrO_2–973R (Scheme S1B), and UV/Visible light irradiation (Figure S15) reached 350 ± 8 K and behaved very similarly to Figure 6, irrelevant to reactants.

To identify the origin of photocatalytic CO reduction in this study, control thermal reaction tests were performed using Co (7.5 wt %)–ZrO_2–973R, ^{13}CO, and H_2 at a reaction temperature between 363 and 423 K (Table S6B). The total formation rate at 350 K was lower by a factor of 71 000 compared to that under UV/Visible irradiation (Scheme 1D and Table 1i), wherein the Co nanoparticles reached 350 K during the CO photoreduction test (Figure S15). This indicates that simple thermal catalysis did not occur solely owing to heat transformed from UV/Visible light energy. Similarly, the total formation rate at 362 K using Co (7.5 wt %)–ZrO_2–823R as evaluated for Co (7.5 wt %)–ZrO_2–973R (Figure 6), $^{13}CO_2$, and H_2 was lower by 200 times compared to that under UV/Visible irradiation (Table S6A and Scheme 1D). The $C_{2,3}$ HC formation was especially suppressed in the thermal reaction, suggesting different reaction pathways under UV/Visible light irradiation (SI, *3.1. Kinetic Results*). The higher apparent activation energy (E_{act}) from CO (151 kJ mol^{-1}) compared to that from CO_2 (83.4 kJ mol^{-1}) contradicts the possibility of higher E_{act} from CO_2 to CO that then follow common pathway. Instead, the fact suggests that CO followed a different thermal pathway from that from CO_2, related to the difference of photocatalytic pathways between Scheme 1A and B.

Reaction Mechanism. FTIR spectroscopy investigated the specific photocatalytic reaction mechanism, starting

from the conversion of CO to C_2H_4 and C_3H_6 using the optimal Co (7.5 wt %)–ZrO_2–973R photocatalyst (Scheme S1B). Analysis of the $^{13}C/^{12}C$ isotopic distribution of the photocatalytic products, generated from $^{13}CO_2$ and ^{13}CO as starting materials (Table S4b–i) and $^{13}CO_2$ exchange reaction (Figure 4), revealed that a part of the $^{12}CO_2$ initially adsorbed from the air onto $Vo^{\bullet\bullet}$ sites at the ZrO_2 surface (one per the area of 61 nm^2) remained after pretreatment under H_2. Subsequently, this $^{12}CO_2$ was then incorporated into the reaction pathway toward HCs (Scheme 1B–a). Migration of $^{12}CO_2$ from $Vo^{\bullet\bullet}$ sites to the surface of Co^0 nanoparticles and its reaction with the surface (Eq. 6) demonstrated by the presence of ^{12}CO stretching vibration ($\nu^{12}CO$) peaks observed at 2142 and 2126 cm^{-1} (Figure 7A-a) under ^{13}CO and H_2:

$$^{12}CO_2 + 2Co^0 \rightleftharpoons O^{12}C{-}Co^{II}O \quad (6)$$

A minor part of the CO formed on the Co^{II} site in Eq. 6 further moved laterally (Figure 5A2) to the Co^0 site ($\nu^{12}CO$ 2028 cm^{-1}, Figure 7A–a). Because ^{13}CO was not in direct equilibrium with $^{12}CO_2$ at the $Vo^{\bullet\bullet}$ sites, species derived from ^{13}CO were not observed at 0 h under ^{13}CO and H_2 (Scheme 1B and Figure 7A–a and B–a).

When the UV/Visible light irradiation started, leading to a gradual decrease in the $\nu^{12}CO$ peak intensity on Co^{II} sites, the corresponding $\nu^{12}CO$ peak on the Co^0 site observed at 2028 cm^{-1} progressively grew (Figure 7A–b and c). It was followed by a progressive increase in the isotopically-labeled terminal and bridging $\nu^{13}CO$ peaks observed at 1978, 1921, 1874, and 1839 cm^{-1} (Figure 7A–c and d),[45] demonstrating that the ^{12}CO species derived from $^{12}CO_2$ adsorbed at $Vo^{\bullet\bullet}$ site when the light was turned on (0 h) were gradually replaced by gas phase ^{13}CO (0–12 h), with ^{13}CO on Co^0 sites becoming the major species at 34 h under light (Figure 7A–d and Scheme 1B–b).

However, the isotopic ratio of the $\nu^{12}CO/\nu^{13}CO$ peak intensity in FTIR (Figure 7A–b and c) and the ratios of $^{12}C_2H_4/(^{12}C_2H_4+{}^{13}C_2H_4)$ and $^{12}CH_4/(^{12}CH_4+{}^{13}CH_4)$ (7.9 mol %, Tables 1i and S4i; Figure 7A–c and d) obtained from gas chromatography–mass spectrometry (GC–MS) were significantly greater than ^{12}CO ratio in reagent (1 %). This discrepancy can be explained if the ^{13}CO adsorbed on Co^0 sites was in equilibrium with $^{12}CO_2$ on $Vo^{\bullet\bullet}$ site at ZrO_2 surface (Scheme 1B–a; Eq. 6 and Figure 7A–a–d), and the CO adsorbed on Co^0 sites should be the intermediate species toward HCs (Scheme 1B–b).

Synchronized with the growth of the $\nu^{12}CO$ peak (Figure 7A-b–d), the antisymmetric and symmetric vibration of $^{12}CH_2$ ($\nu_{as}{}^{12}CH_2$ and $\nu_s{}^{12}CH_2$) peaks increased at 2936 and 2858 cm^{-1}, respectively, accompanied by weak vibration peaks for $^{12}CH_3$ ($\nu_{as}{}^{12}CH_3$ 2958 cm^{-1}; $\nu_s{}^{12}CH_3$ 2876 cm^{-1}) under ^{13}CO, H_2, and UV/Visible light (Figure 7B–c). Then, following the isotopic replacement by multiple $\nu^{13}CO$ peaks (Figure 7A–b–d), the CH_2/CH_3 vibrational pairs of $\nu_{as}{}^{12}CH_n$ and $\nu_s{}^{12}CH_n$ ($n=2$, 3) progressively shifted to the corresponding ^{13}C-isotopic pairs of $\nu_{as}{}^{13}CH_n$ and $\nu_s{}^{13}CH_n$ (2927 and 2850 cm^{-1} when $n=2$ and 2948 and 2869 cm^{-1} when $n=3$, respectively, Figure 7B–d). Although the stretching vibration peak intensity ratio of CH_2/CH_3 in FTIR was almost constant at 3:1 during the 34-hour photocatalytic test (Figure 7C), the major product obtained using GC–MS transformed consecutively transformed from $^{13}C_2H_4$ to $^{13}CH_4$ (Figure 7D). This indicates that the ratio of CH_x to H adsorbed at a specific local site, e.g., the interface site between Co^0 and the ZrO_2 surface, determined the product selectivity (Scheme 1B–b–e). In contrast, the $^{12}CO_3$ at the ZrO_2 surface was replaced by $^{13}CO_3$ species (1513 and 1308 cm^{-1}), while bidentate ^{13}C-formate at the ZrO_2 surface gradually increased (1523 and 1344 cm^{-1})[32] until 34 h of reaction under ^{13}CO, H_2, and UV/Visible light (Figure S16), both irrelevant to HC generation over the Co^0 surface.

Then, the Co (7.5 wt %)–ZrO_2–973R photocatalyst subjected to vacuum and the UV/Visible light irradiation. In contrast to the quick disappearance of all the weakly adsorbed CO peaks (Figure 7A–e and f), approximately half of the reaction intermediate CH_2 and CH_3 species remained at 2 h under vacuum (Figure 7B–e, f and C), consistent with the HC preference using this photocatalyst.

Spin-polarized periodic DFT + U calculations were conducted using the Vienna Ab initio Simulation Package code

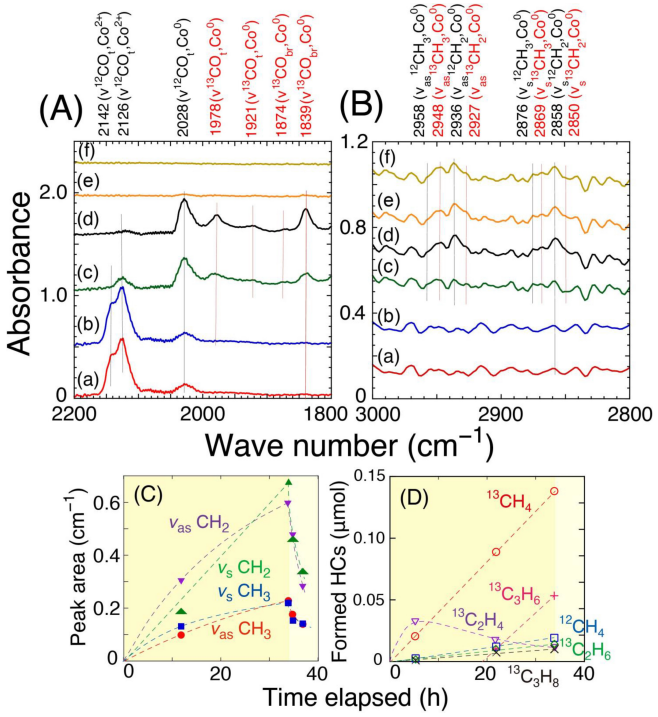

Figure 7. FTIR monitoring of reaction intermediates using the Co (7.5 wt %)–ZrO_2–973R photocatalyst (71 mg) in the (A) carbonyl and (B) C–H stretching vibration regions and the peak assignments. The reaction conditions were as follows: (a) under ^{13}CO (2.3 kPa) and H_2 (2.3 kPa) in the dark for 2 h, (b–d) under ^{13}CO (2.3 kPa), H_2 (2.3 kPa), and UV/Visible light irradiation at 0 h (b), 12 h (c), and 34 h (d), and (e, f) under vacuum and UV/Visible light irradiation at 0 h (e) and 2 h (f). (C) The time course of CH_2 and CH_3 stretching vibration peak intensity (including convolution of ^{13}C and ^{12}C peaks) by FTIR and (D) the corresponding time course of photocatalytic products monitored using GC–MS.

version 6.2.1[46] (SI, *2. Experimental Section*). CO_2 was adsorbed at the $Vo^{\bullet\bullet}$ site (Scheme 1A–a and Figure S8A and B).[31] When H was provided, the adsorbed CO_2 transformed to OCOH with an E_{act} of 1.3 eV (Scheme 2A–b). If the $Vo^{\bullet\bullet}$ site neighbored a Co^0 site, the terminal O atom of the OCOH group occupied the $Vo^{\bullet\bullet}$ site (species b), and the COH moiety hopped onto the metallic Co^0 atom with an E_{act} of 0.28 eV (species c). A very similar reaction mechanism was also proposed for Pd–ZrO_2.[47] The population of $Vo^{\bullet\bullet}$ sites adjacent to the Co^0 nanoparticle was anticipated to be relatively higher compared to the mean population of one $Vo^{\bullet\bullet}$ per ZrO_2 surface area of 61 nm^2 (Table S5b). This is because the Fermi level of Co (work function 5.0 eV)[48] is lower than the energy level of $Vo^{\bullet\bullet}$ in ZrO_2,[31] enabling electron acceptance,[49] thereby facilitating the generation of $Vo^{\bullet\bullet}$ sites neighboring to Co^0 nanoparticles.

Throughout the pathway to CH_4, the hydrogenation to OCOH required the highest E_{act} of 1.3 eV, followed by the E_{act} of 0.93 eV for CH_3 hydrogenation, and 1.2 eV for OH hydrogenation by the elimination at the interface (Scheme 2A–a, b, d, and e, *Methyl route*), thereby supporting the preferential formation of CH_4 from CO_2 (Table 1b–e). The regeneration energy of the $Vo^{\bullet\bullet}$ site can be minimized to 1.7 eV by replacing H_2O with CO_2 at the $Vo^{\bullet\bullet}$ site.[31] C_2H_6 was formed via the *Ethene route* (Scheme 2A′) as a by-product, preferably via C_2H_4 (E_{act} of 0.70 eV) rather than the coupling of two CH_3 (E_{act} of 1.0 eV; Scheme 2A–d, Figure S4, and Eq. S1), different from the situation using Ni–ZrO_2 photocatalyst, where CH_4 was exclusively formed.[31] The dissociation of $HOCH_2$ into hydroxy and CH_2 at the interface was also suggested (Scheme 2A), in contrast to considerably stable HOCH and dissociation on the Ni^0 surface.[31]

The reaction route of CO photoreduction, especially to C_2H_4, was also investigated by DFT calculations. In contrast to CO_2 adsorption at the $Vo^{\bullet\bullet}$ site of the ZrO_2 surface,[31–33] CO is adsorbed on the Co^0 site (the adsorption energy (E_{ads}) of 2.23 eV; Schemes 1B–b and 2B–b), followed by the formation of CHO and HCOH species at the interface of the ZrO_2 surface and Co^0 (Schemes 1B–c and 2B–c). It is energetically advantageous when the hydroxy group fills the neighboring $Vo^{\bullet\bullet}$ site to form CH (Schemes 1B–d and 2B–d). In the following *Methyl route*, the barrier for CH_3 hydrogenation to form CH_4 is highest (0.75 eV). In comparison, the *Ethene route* via the coupling of CH_2 was more favorable (E_{act} of 0.70 eV, Scheme 2B–e and f), which aligns with the specific formation of $^{13}C_2H_4$ and $^{13}C_3H_6$ from CO within the first 0–4 h of the reaction (Table 1g–i). The isotopic shuffling of $^{13}C/^{12}C$ was also plausible between CO adsorbed on the Co^0 surface and $^{12}CO_2$ adsorbed at the $Vo^{\bullet\bullet}$ sites from the air (Scheme 1B–a–c).

The advantageous CO adsorption in the first stage transitions to competitive adsorption of CO (E_{ads} of 1.36 eV) and H (E_{ads} of 1.32 eV; Scheme 2B–b and b′) in the second step of consecutive photocatalysis. The increased population of H on Co^0 sites kinetically explains the transition to form C_{1-3} paraffin and C_3H_6 after 4 h of the reaction (Figures 2 and S3). In contrast, under CO_2 and H_2, H adsorption on

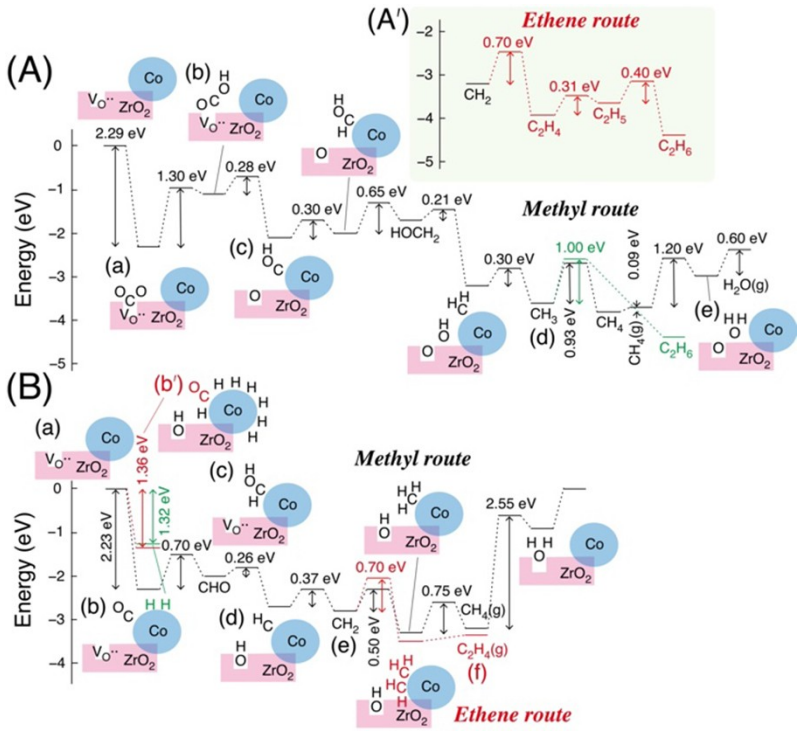

Scheme 2. Energy Diagram over Monoclinic ZrO_2 (1 1 1) Surface Combined with Co_{19} Cluster Exposing hcp (0 1 0) Surface Calculated (A) under CO_2 and H_2 and (B) under CO and H_2. Ethene Route Was Also Drawn in (A′) and (B) Compared to Methyl Route. Three-Dimensional Illustration of Each Species Is Presented in Scheme S2.

Co^0 is rarely hampered by CO_2, and CH_2 is easily transformed to CH_3 (E_{act} of 0.30 eV, Scheme 2A–d) throughout the photocatalytic tests (SI, *3.3. DFT Calculations*).

Selective $C_{2,3}$ olefin formation proceeded during intial 4 h of reaction (Figures 2 and 3) while on later stage, CH_4 was a major product with minor C_2H_6, C_3H_6, and C_3H_8 (Figure 2). This contrast was understandable if we assume the adsorbed CO/H balance on Co^0 surface decreased as the time elapsed (Scheme 2B–b and b′). Compared to the two different stages of reaction starting from CO, COH species hopped from $Vo^{\bullet\bullet}$ site to Co^0 surface followed by down-hill steps mostly to CH_4 (Scheme 2A–c and d). The consecutive reaction steps on separated sites on ZrO_2 and Co^0 starting from CO_2 proceeded efficiently (Scheme 2A) compared to competitive steps mostly on Co^0 starting from CO (Scheme 2B and Figure 7).

Photocatalytic CO_2 reduction has been proposed to proceed via various ways, including the coupling of two CO molecules to form C_2H_4 at $Vo^{\bullet\bullet}$ sites of TiON,[16] In–(S vacancy)–Bi,[21] and $Cu^{\delta+}$ sites,[25] the reaction of CO with CHOH to form OC–CHOH and then to C_2H_4 at Cu^I–Cu^{II} sites,[20] and the reaction of CO with COH to form C_2H_4 at $In_{2.77}S_4$ surfaces[23] (Table S1j, n, o, q, and s). However, herein, CO did not directly participate in forming the C–C bond. Instead, the coupling of two species to form C_2H_4 at the $FeCoS_2$ surface,[22] the coupling of two CHOs to form CH–CHOH and then to C_2H_4 at the Fe–N surface,[24] and the coupling of CH_3 with CH_3 or C_2H_5 to form C_2H_6 and C_3H_8 at Cu_2O[7] and Cu surfaces,[9] have been reported. Additionally, the coupling of CH_3 at TiO_2 surfaces[11–12] and Au surfaces[13] to form C_2H_6 has been reported via C–C formation, involving oxygenate and/or HC intermediates (Table S1a, c, e–g, p, and r). In these reports, the combination of reduced active sites with partially oxidized sites resembles the Co^0 site and the neighboring $Vo^{\bullet\bullet}$ site at the ZrO_2 surface to form $C_{2,3}$-olefins from CO (Scheme 1B) and C_{1-3}-paraffin from CO_2 (Scheme 1A).

Photocatalytic CO_2 Reduction Using H_2O. Compared with the photosynthesis of $^{13}C_2H_6$ and $^{13}C_3H_8$ from $^{13}CO_2$ and H_2 (3.7–4.5 $\mu mol\,h^{-1}\,g_{cat}{}^{-1}$; Table 1c and d and Figure 8A) and the photosynthesis of $^{13}C_2H_4$ and $^{13}C_3H_6$ from ^{13}CO and H_2 (5.5–5.9 $\mu mol\,h^{-1}\,g_{cat}{}^{-1}$; Table 1g and i and Figure 8B), CO_2 photoreduction was attempted using H_2O as a one-step sustainable reaction under reaction conditions similar to those reported in Table S1.[7–25]

The key factors for paraffin synthesis were the metallic Co^0 surface and the adsorbed H species on the Co^0. Using the Co–ZrO_2–823R photocatalyst (Scheme S1A) and swiftly evacuating gas-phase H_2, H_2O (2.2 kPa) served as a reductant for CO_2 (2.3 kPa) under UV/Visible light irradiation to form $^{13}C_2H_6$ and $^{13}C_3H_8$ at a rate of 0.21 $\mu mol\,h^{-1}\,g_{cat}{}^{-1}$ (Table 1f and Figures 8C and S17). Conversely, O_2 was not formed above the detection limit because the formed O_2 reacted with adsorbed H species on the Co surface to regenerate H_2O at the solid/gas interface.

This challenge was addressed using liquid H_2O for the photocatalytic CO_2 conversion to release O_2 from the surface. C_2H_6 and C_3H_8 were photogenerated at rates of 2.0–2.7 $\mu mol\,h^{-1}\,g_{cat}{}^{-1}$ at a steady state for 48 h (Figures S18A and B), with up to 60 mol % of $C_{2,3}$ HC formation using H_2 (Table 1c, k, and l and Figure 8A and D), accompanied by O_2 formation at the rates higher than 66 $\mu mol\,h^{-1}\,g_{cat}{}^{-1}$ using Co–ZrO_2–823R and −973 R photocatalysts. The relatively high formation rates to $C_{2,3}$ HCs compared to that to CH_4 (31–60 mol %; Table 1k and l) were attributed to competitive adsorption of C-species and H_2O on Co^0, rather than the 1.4–1.8 mol % using H_2 preferably adsorbed on Co^0 (Table 1c and d). However, sufficiently high light intensity (222 mW cm^{-1}) was needed for CO_2 photoconversion in H_2O (Tables 1j, l and S8a–e; SI, *3.4. Photocatalytic Conversion of CO_2 Using H_2O*).

$^{13}CO_2$ (2.3 kPa) photoreduction using D_2O (2.2 kPa), H_2 (21.7 kPa), and Co–ZrO_2–823R formed ^{13}C-methane with a D ratio of 9.2 mol %, which agrees with a D ratio in the

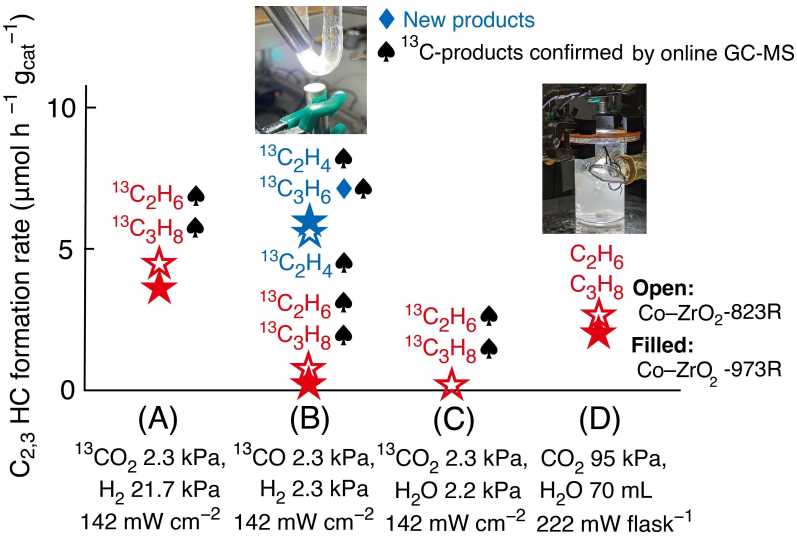

Figure 8. Summary of major findings of $C_{2,3}$ photosynthesis rates using (A, C) $^{13}CO_2$, (B) ^{13}CO, (D) CO_2, (A, B) H_2, (C, D) H_2O, and Co (7.5 wt %)–ZrO_2–823R (open symbol) or −973R (filled symbol) photocatalyst irradiated by UV/Visible light at each intensity.

reactants (9.1 mol %; Figure S19 and Table S7b; SI, *3.5. Photocatalytic Conversion of $^{13}CO_2$ Using D_2O*). This suggests that D_2O and H_2 reached equilibrium more rapidly and were shuffled over Co^0 more efficiently than the progressive hydrogenation steps to $C_{2,3}$ paraffin common under either H_2 or H_2O (Scheme 1A–a–d). Such a photocatalytic pathway from CO_2 to $C_{2,3}$ paraffin using either H_2 or H_2O[7–15] and the photoformation from CO to C_3H_6 have been rarely reported.

This study paves the way to precisely explore further active photocatalysts to selectively produce $C_{2,3}$-HCs utilizing unsaturated/lower-dimensional semiconductors to regenerate the $Vo^{\bullet\bullet}$ sites with an E_{act} of <2.6 eV (Scheme 2B). This can be achieved in combination with metal nanoparticles/single atoms using either H_2 or H_2O, surpassing the capabilities of recent photocatalysts (Table S1).[7–25]

Conclusions

The Co (7.5 wt %)–ZrO_2–823R photocatalyst formed $C_{1–3}$ paraffin at a total formation rate of 330 ± 20 μmol h^{-1} $g_{cat}{}^{-1}$ using CO_2 and H_2. In contrast, Co (7.5 wt %)–ZrO_2–973R formed C_2H_4 and C_3H_6 at a total formation rate of 6.0 ± 0.6 μmol h^{-1} $g_{cat}{}^{-1}$ with an olefin selectivity of 70 mol % using CO and H_2. CO_2 was adsorbed on the $Vo^{\bullet\bullet}$ sites at the ZrO_2 surface, and the intermediate COH species hopped onto the Co^0 surface, where it was progressively hydrogenated to form CH_3 and/or CH_2 species, which subsequently coupled to form $C_{1–3}$ paraffin. Conversely, CO adsorbed on Co^0 was hydrogenated to form HOCH and was most effectively dissociated to CH at the interface with the ZrO_2 surface comprising the $Vo^{\bullet\bullet}$ site. Preferential CO adsorption and favorable CH_2 coupling until 4 h were followed by the competitive adsorption of CO and H on Co^0 sites, resulting in consecutive CH_4 and C_3H_6 formation. Predominant photocatalytic formation of C_2H_4 and C_3H_6 (61–87 mol %) was achieved from CO after repeated tests for 4–10 h, followed by evacuation. The dual mechanism involved electron donation from $Vo^{\bullet\bullet}$ to OCOH/HOCH species using CO_2/CO, followed by consecutive hydrogenation steps on the Co^0 surface at 362/350 K, facilitated by UV/Visible light energy, at a rate of 200/71 000 times higher than that observed via a thermal reaction at 362/350 K, respectively, without light. CO_2 photoreduction to C_2H_6 and C_3H_8 was possible in H_2O (l) to release O_2 from the surface via a very similar pathway involving $CH_{3/2}$ activation on Co^0.

Acknowledgements

The authors are grateful for the financial support from the Grant-in-Aid for Scientific Research B (24K01522, 20H02834, YI) and C (20K05643, KN) from the Japan Society for the Promotion of Science and from the Establishment of University Fellowships toward the Creation of Science and Technology Innovation from the Japan Science and Technology Agency (JPMJFS2107, KH). X-ray absorption experiments were performed with the approval of the Photon Factory Proposal Review Committee (2022G527, 2021G546, 2020G676, 2019G141). A part of the computation was performed using the facilities of Institute for Solid State Physics, University of Tokyo. The authors thank Dr. Tetsuo Higuchi, JEOL for GC–MS optimization and Yusuke Futamata, Shunsuke Watanabe, and Mai Ichimura, Shimadzu for XPS measurements. The authors would like to thank Enago (www.enago.jp) for the language review.

Conflict of Interest

The authors declare no conflict of interest.

Data Availability Statement

The data that support the findings of this study are available from the corresponding author upon reasonable request.

Keywords: Photocatalyst · Cobalt · Carbon dioxide · Paraffin · Ethene

[1] Y. Izumi, *Coord. Chem. Rev.* **2013**, *257*, 171–186.
[2] Y. Izumi, *ACS Books Advances in CO_2 Capture, Sequestration, and Conversion*, (F. Jin, L.-N. He, Y. H. Hu, Eds.), ACS Symposium Series, ACS Publications, **2015**, *1194(1)*, 1–46.
[3] J. Albero, Y. Peng, H. García, *ACS Catal.* **2020**, *10*, 5734–5749.
[4] S. Nitopi, E. Bertheussen, S. B. Scott, X. Liu, A. K. Engstfeld, S. Horch, B. Seger, I. E. L. Stephens, K. Chan, C. Hahn, J. K. Nørskov, T. F. Jaramillo, I. Chorkendorff, *Chem. Rev.* **2019**, *119*, 7610–7672.
[5] H.-Q. Liang, T. Beweries, R. Francke, M. Beller, *Angew. Chem. Int. Ed.* **2022**, *61*(19), e202200723.
[6] Y. Lum, T. Cheng, W. A. Goddard III, J. W. Ager, *J. Am. Chem. Soc.* **2018**, *140*(30), 9337–9340.
[7] N. Li, B. Wang, Y. Si, F. Xue, J. Zhou, Y. Lu, M. Liu, *ACS Catal.* **2019**, *9*(6), 5590–5602.
[8] H. Ou, G. Li, W. Ren, B. Pan, G. Luo, Z. Hu, D. Wang, *J. Am. Chem. Soc.* **2022**, *144*(48), 22075–22082.
[9] H. Park, H.-H. Ou, A. J. Colussi, M. R. Hoffmann, *J. Phys. Chem. A* **2015**, *119*(19), 4658–4666.
[10] W. Kim, T. Seok, W. Choi, *Energy Environ. Sci.* **2012**, *5*(3), 6066–6070.
[11] S. Sorcar, J. Thompson, Y. Hwang, Y. H. Park, T. Majima, C. A. Grimes, J. R. Durrant, *Energy Environ. Sci.* **2018**, *11*(11), 3183–3193.
[12] W. Tu, Y. Zhou, Q. Liu, S. Yan, S. Bao, X. Wang, M. Xiao, Z. Zou, *Adv. Funct. Mater.* **2013**, *23*(14), 1743–1749.
[13] Y. Wang, J. Zhao, Y. Liu, G. Liu, S. Ding, Y. Li, J. Xia, H. Li, *J. Colloid Interface Sci.* **2022**, *616*, 649–658.
[14] X. Zhang, F. Han, B. Shi, S. Farsinezhad, G. P. Dechaine, K. Shankar, *Angew. Chem. Int. Ed.* **2012**, *51*(51), 12732–12735.
[15] Q. Chen, X. Chen, M. Fang, J. Chen, Y. Li, Z. Xie, Q. Kuang, L. Zheng, *J. Mater. Chem.* A **2019**, *7*(3), 1334–1340.
[16] B. Ni, G. Zhang, H. Wang, Y. Min, K. Jiang, H. Li, *Angew. Chem. Int. Ed.* **2023**, *62*(6), e202215574.
[17] L. Yu, G. Li, X. Zhang, X. Ba, G. Shi, Y. Li, P. K. Wong, J. C. Yu, Y. Yu, *ACS Catal.* **2016**, *6*(10), 6444–6454.
[18] K. Adachi, K. Ohta, T. Mizuno, *Solar Ener.* **1994**, *53*(2), 187–190.

[19] M. M. Gui, W. M. P. Wong, S.-P. Chai, A. R. Mohamed, *Chem. Eng. J.* **2015**, *278*, 272–278.
[20] S. Chakraborty, R. Das, M. Riyaz, K. Das, A. K. Singh, D. Bagchi, C. P. Vinod, S. C. Peter, *Angew. Chem. Int. Ed.* **2023**, *62*(9), e202216613.
[21] K. Yan, D. Wu, T. Wang, C. Chen, S. Liu, Y. Hu, C. Gao, H. Chen, B. Li, *ACS Catal.* **2023**, *13*(4), 2302–2312.
[22] Y. Wu, Q. Chen, J. Zhu, K. Zheng, M. Wu, M. Fan, W. Yan, J. Hu, J. Zhu, Y. Pan, X. Jiao, Y. Sun, Y. Xie, *Angew. Chem. Int. Ed.* **2023**, e202301075.
[23] R. Das, R. Paul, A. Parui, A. Shrotri, C. Atzori, K. A. Lomachenko, A. K. Singh, J. Mondal, S. C. Peter, *J. Am. Chem. Soc.* **2023**, *145*(1), 422–435.
[24] F. Guo, R.-X. Li, S. Yang, X.-Y. Zhang, H. Yu, J. J. Yuban, W.-Y. Sun, *Angew. Chem. Int. Ed.* **2023**, *62*, e202216232.
[25] T. Wang, L. Chen, C. Chen, M. Huang, Y. Huang, S. Liu, B. Li, *ACS Nano* **2022**, *16*(2), 2306–2318.
[26] Y. Wang, E. Chen, J. Tang, *ACS Catal.* **2022**, *12*(12), 7300–7316.
[27] L. Liao, G. Xie, X. Xie, N. Zhang, *J. Phys. Chem. C* **2023**, *127*(6), 2766–2781.
[28] M. Hu, J. Liu, S. Song, W. Wang, J. Yao, Y. Gong, C. Li, Y. Li, Y. Li, X. Yian, Z. Fang, H. Xu, W. Song, Z. Li, *ACS Catal.* **2022**, *12*(5), 3238–3248.
[29] Y.-L. Zhang, L. Zhou, X.-C. Sun, Q. Zhang, H.-J. Yin, P. Du, X.-F. Yang, Y.-W. Zhang, *J. Phys. Chem. C* **2022**, *126*(6), 3017–3028.
[30] J.-X. Liu, H.-Y. Su, D.-P. Sun, B.-Y. Zhang, W.-X. Li, *J. Am. Chem. Soc.* **2013**, *135*(44), 16284–16287.
[31] K. Hara, M. Nozaki, T. Hirayama, R. Ishii, K. Niki, Y. Izumi, *J. Phys. Chem. C* **2023**, *127*(4), 1776–1788.
[32] H. Zhang, T. Itoi, T. Konishi, Y. Izumi, *Angew. Chem. Int. Ed.* **2021**, *60*(16), 9045–9054.
[33] H. Zhang, T. Itoi, T. Konishi, Y. Izumi, *J. Am. Chem. Soc.* **2019**, *141*(15), 6292–6301.
[34] T. He, D. Chen, X. Jiao, Y. Wang, Y. Duan, *Chem. Mater.* **2005**, *17*(15), 4023–4030.
[35] N. A. M. Barkakat, M. S. Khil, F. A. Sheikh, H. Y. Kim, *J. Phys. Chem. C* **2008**, *112*(32), 12225–12233.
[36] N. Ahmed, Y. Shibata, T. Taniguchi, Y. Izumi, *J. Catal.* **2011**, *279*, 123–135.
[37] H. Putz, K. Brandenburg, *Diamond version 3.2k* Crystal Impact, Bonn, Germany, **2014**.
[38] W. Jauch, M. Reehuis, H. J. Bleif, F. Kubanek, *Phys. Rev. B* **2001**, *64*, 052102.
[39] https://www.webelements.com/cobalt/crystal_structure.html (checked on June *21* **2024**.
[40] B. J. Kip, B. M. Duivenvoorden, D. C. Koningsberger, R. Prins, *J. Catal.* **1987**, *105*, 26–38.
[41] G. Beni, P. M. Platzman, *Phys. Rev. B* **1976**, *14*, 1514–1518.
[42] E. Sevillano, H. Meuth, J. J. Rehr, *Phys. Rev. B* **1979**, *20*, 4908–4911.
[43] B. H. Billings, H. P. R. Frederikse, D. F. Bleil, R. B. Lindsay, R. K. Cook, J. B. Marion, H. M. Crosswhite, M. W. Zemansky, *American Institute of Physics Handbook*, 3rd ed. (D. E. Gray, Ed.), McGraw-Hill, New York, USA, **1972**, 4–115.
[44] M. Hou, M. El Azzaoui, H. Pattyn, J. Verheyden, G. Koops, G. Zhang, *Phys. Rev. B* **2000**, *62*(8), 5117–5128.
[45] T. Liu, D. Xu, M. Song, X. Hong, G. Liu, *ACS Catal.* **2023**, *13*(7), 4667–4674.
[46] G. Kresse, J. Furthmüller, *Phys. Rev. B* **1996**, *54*, 11169–11186.
[47] Y. Li, K. Zheng, Y. Shen, M. Huang, B. Liu, Y. Xu, X. Liu, *J. Phys. Chem. C* **2023**, *127*(12), 5841–5854.
[48] D. R. Lide, T. J. Bruno, et al., *CRC Handbook of Chemistry and Physics*, 96th ed. (W. M. Haynes, Ed.), CRC Press: Boca Raton **2015**, 12–122.
[49] Y. Hinuma, T. Toyao, N. Hamamoto, M. Takao, K. Shimizu, T. Kamachi, *J. Phys. Chem. C* **2020**, *124*(50), 27621–27630.

Manuscript received: June 27, 2024
Accepted manuscript online: September 18, 2024
Version of record online: November 2, 2024